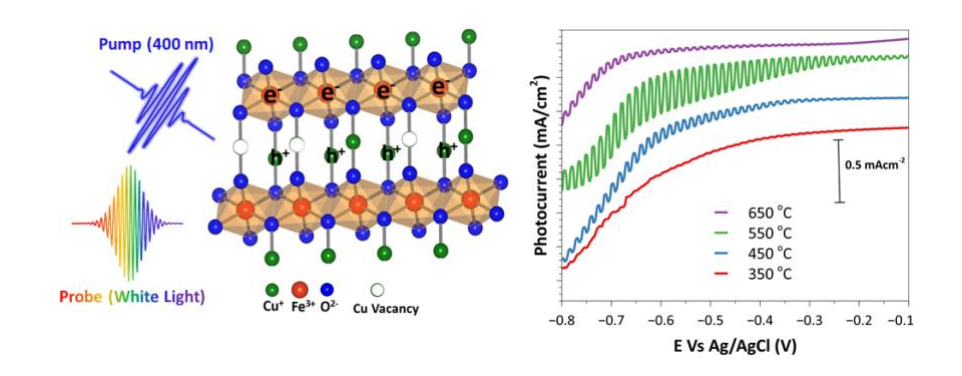
## TABLE OF CONTENTS (TOC) GRAPHICS

The Role of Phase Impurities and Lattice Defects on the Electron Dynamics and Photochemistry of CuFeO<sub>2</sub> Solar Photocathodes

Elizabeth Fugate<sup>1</sup>, Somnath Biswas<sup>1</sup>, Matthew C. Clement<sup>1</sup>, Minkyu Kim<sup>2</sup>, Dongjoon Kim<sup>2</sup>, Aravind Asthagiri<sup>2\*</sup>, and L. Robert Baker<sup>1\*</sup>

- <sup>1</sup> Department of Chemistry and Biochemistry, The Ohio State University, Columbus OH, 43210, USA
- Department of Chemical and Biomolecular Engineering, The Ohio State University, Columbus OH, 43210, USA



In this work we investigate the role of phase impurities and lattice defect states on the electron dynamics and photochemical efficiency of CuFeO<sub>2</sub>. Visible light transient absorption and DFT calculations provide insight on effects of Cu vacancies, O interstitials, and CuO/CuFeO<sub>2</sub> heterostructures on the competition between charge separation and recombination dynamics in this material.

1

# The Role of Phase Impurities and Lattice Defects on the Electron Dynamics and Photochemistry of CuFeO<sub>2</sub> Solar Photocathodes

Elizabeth A. Fugate<sup>1</sup>, Somnath Biswas<sup>1</sup>, Matthew C. Clement<sup>1</sup>, Minkyu Kim<sup>2</sup>, Dongjoon Kim<sup>2</sup>, Aravind Asthagiri<sup>2</sup>( $\boxtimes$ ), and L. Robert Baker<sup>1</sup>( $\boxtimes$ )

<sup>1</sup> Department of Chemistry and Biochemistry, The Ohio State University, Columbus OH, 43210, USA

Received: day month year / Revised: day month year / Accepted: day month year (automatically inserted by the publisher) ©The Author(s) 2010. This article is published with open access at Springerlink.com

#### **ABSTRACT**

CuFeO<sub>2</sub> is a promising photocathode for H<sub>2</sub> evolution and CO<sub>2</sub> reduction reactions. To better understand the complex defect chemistry and role of impurity phases in this material and their effect on the photochemical performance, we employ visible light transient absorption spectroscopy and DFT calculations to investigate the electron dynamics in electrochemically deposited Cu-Fe oxide thin films. Kinetic analysis of carrier lifetime shows a fast, sub-ps contribution to relaxation followed by persistence of a long-lived state to time delays greater than 2 ns. Increasing amplitude of the long-lived state is shown to correlate with the rate of fast initial relaxation, and this is explained in terms of a competition between charge carrier trapping and charge separation. Charge separation in CuFeO<sub>2</sub> occurs via hole thermalization from O 2p to Cu 3d valence band states leading to segregation of electrons and holes across layers in the CuFeO<sub>2</sub> lattice. Correlation between transient absorption measurements and DFT calculations suggest that Cu vacancies enhance photochemical performance by facilitating charge separation kinetics. In contrast, O interstitials are predicted to switch the relative positions of O 2p and Cu 3d valence band states, which would inhibit charge separation by inter-band hole thermalization. Finally, we find no evidence for electron injection from CuFeO<sub>2</sub> to CuO suggesting that charge separation at this heterostructure interface does not play a role in the carrier lifetime or photochemical performance of the catalysts studied here.

# **KEYWORDS**

Delafossite CuFeO<sub>2</sub>, charge-carrier dynamics, transient absorption spectroscopy, Cu vacancy, O interstitial

#### 1 Introduction

Photoelectrochemistry using semiconductor electrodes offers a simple platform for the conversion of sunlight into chemical energy [1]. In this scheme a band gap excitation is used to generate conduction band electrons and valence band holes. Depending

on the band alignment of the semiconductor relative to the redox potential of a reaction of interest, these photo-generated charge carriers may drive an electrochemical reaction at the semiconductor surface. In photoelectrochemistry, it is common for the semiconductor to serve as both the light absorber as well as the catalyst [2-4]. This means that

<sup>&</sup>lt;sup>2</sup> Department of Chemical and Biomolecular Engineering, The Ohio State University, Columbus OH, 43210, USA

photochemical efficiency is a complex function of a wide range of materials properties, including light absorption, carrier lifetime, carrier mobility, surface reaction kinetics, and catalyst stability [2, 5-7]. Consequently, a search for materials capable of enabling sunlight to fuel conversion in a robust, economic, and efficient platform has become one of the major challenges toward enabling a sustainable energy economy.

Transition metal oxides are earth-abundant and offer a number of benefits for photoelectrochemical applications, including strong absorption in the solar spectrum and stability during photoelectrochemical reaction [2, 3, 8-10]. In particular, delafossite CuFeO<sub>2</sub> has emerged as a promising metal oxide due to its relatively small band gap (1.5 eV) and p-type conductivity, and this material has been shown to catalyze both H<sub>2</sub> evolution and CO<sub>2</sub> reduction[9, 11-14]. However, photocurrent densities in CuFeO<sub>2</sub> are typically limited to 0.4 mA/cm<sup>2</sup> or less[6, 10, 12, 15-17].

Many fundamental questions related to the complex defect chemistry in compound semiconductors remain unanswered, even though it is generally accepted that defect states significantly influence photoelectrochemical performance [18-22]. Both interstitial anions and metal vacancies are commonly cited as p-type donors in compound semiconductors, including both III-V and II-V materials [20, 23-25]. It is important to note that in most synthesis and posttreatment processes designed to control dopant concentration, these two types of defects trend together, making it difficult to determine the independent contribution of each to the resulting material performance. In the case of CuFeO2 and related delafossite phases, a number of studies have investigated the effects of defect chemistry on photoelectrochemical performance, and these studies provide insight into the respective roles of O interstitials as well as Cu vacancies [12, 20, 21, 26, 27].

Bocarsly and co-workers investigated the effects of Mg doping in CuFeO<sub>2</sub>, where Mg<sup>2+</sup> substitutes Fe<sup>3+</sup> in the delafossite lattice and serves as a p-type donor [10, 12]. In addition, they also prepared Cu-deficient CuFeO<sub>2</sub> to compare the effects of Cu vacancy formation with Mg doping. Although both donors increase the material conductivity, they found no correlation between carrier concentration, carrier

mobility, and photoelectrochemical efficiency. Rather they observed that cathodic photocurrent showed saturation behavior at applied bias below –0.46 V (RHE), indicating that photocurrent density is likely limited by charge carrier recombination kinetics.

In another study, it was shown that post-processing of CuFeO<sub>2</sub> photocathodes by microwave annealing increases the photocurrent density to greater than 0.6 mA/cm<sup>2</sup> [21]. This enhancement, which could not be produced by traditional thermal annealing, was observed to correlate with oxidation of bulk Cu as probed by x-ray absorption fine structure analysis. From this evidence it was hypothesized that the intercalation of interstitial O into the CuFeO<sub>2</sub> lattice resulted in enhanced photocurrent densities.

It is important to note that catalysts showing high performance often consist of mixed phases containing various internal heterostructures in addition to multiple types of defects. Specifically, a number of studies have hypothesized that a type heterojunction may form at the CuO/CuFeO2 boundary in mixed phase copper iron oxide and that this heterojunction facilitates charge separation as electrons inject from CuFeO2 into CuO and holes accumulate in the CuFeO2 phase [28-31]. This charge separation, if it occurs, would presumably result in increased carrier lifetime with CuO serving as the electrochemically active phase. However, to date no spectroscopic evidence has been provided confirming charge injection between CuO and CuFeO2 in these mixed phase systems. We have previously used extreme ultraviolet reflection absorption (XUV-RA) and visible light TA spectroscopy to investigate the carrier dynamics in CuFeO2 [32]. In that study, we find that photoexcitation of CuFeO2 can be described as a charge transfer transition where electron transfer occurs from O 2p valence band states to Fe 3d conduction band states. This ligand to metal charge transfer state quickly relaxes via hole thermalization from O 2p to Cu 3d valence band states in approximately 0.5 ps, resulting in a metal-metal charge transfer excited state. Correlations between ultrafast XUV measurements, which are sensitive to oxidation state changes of specific elements, with visible light TA measurements of the same system, provided a reliable interpretation of the visible TA spectrum. Building on this understanding, we now

extend visible light TA studies to copper-iron oxide mixed phase samples with a range of defect state densities to investigate the correlation between defect states, carrier lifetimes, and photo-catalytic activity in these materials.

In order to provide a better understanding of the complex defect chemistry in mixed-phase copper iron oxide and its effect on carrier lifetime and catalyst performance, in this study we employ visible light TA spectroscopy to investigate the excited state lifetimes and photophysics in electrochemically deposited copper iron oxide catalysts annealed at temperatures spanning 350 to 650 °C. Spectroscopic results together with DFT calculations enable us to differentiate between the possible effects of Cu interstials CuO/CuFeO<sub>2</sub> vacancies, O heterostructures on the carrier lifetime and corresponding photoelectrochemical efficiency of this material.

Three conclusions can be drawn from the experimental and computational work presented here: First, these results indicate that Cu vacancies improve photoelectrochemical efficiency by facilitating ultrafast charge separation. This occurs as valence band holes thermalize from O 2p to hybridized Cu 3d valence band states, leading to interlayer charge separation of electrons and holes, resulting in increased carrier lifetimes. Second, we find that the frontier valence band orbital changes from Cu 3d to O 2p upon introduction of interstitial O. This switch in the position between Cu 3d and O 2p states precludes hole thermalization to Cu 3d orbitals, which prevents spatial charge separation and limits the overall efficiency. Finally, we observe that photoexcited electrons reside primarily in Fe 3d conduction band states to lifetimes greater than 2 ns, indicating that interfacial charge transfer from CuFeO2 to CuO is not responsible for enhanced carrier lifetimes in the catalysts studied here.

# 2 Experimental and Computational Details

#### 2.1 Electrochemical deposition

The catalyst deposition procedure is similar to previously reported methods [13, 33, 34]. To summarize, all of the catalysts were prepared by

electrodeposition in a single-compartment electrochemical cell using a Ag/AgCl aqueous reference electrode with a Pt counter electrode. Fluorine-doped tin oxide (FTO) substrates were cut into 2 × 1 cm square pieces for use as working electrodes. During electrodeposition the temperature was controlled at 80 °C using an oil bath. Prior to deposition the FTO glass was cleaned with piranha solution (3 parts sulphuric acid to 1 part hydrogen peroxide) at 70 °C for 20 minutes. After piranha cleaning, the substrates were rinsed 10 times in 18  $M\Omega$ ·cm Millipore water (Synergy® UV Remote Water System) Purification before electrodeposition. Applied potentials were controlled using a Biologic® SP-50 potentiostat.

All chemicals were purchased from Sigma-Aldrich and used without further purification. Deposition solutions were made by dissolving 0.01 M CuNO<sub>3</sub>, 0.03 M FeClO<sub>4</sub>, and 0.1 M KClO<sub>4</sub> in DMSO such that the Cu:Fe ratio in the plating solution was 1:3. A potential of -0.3 V vs. Ag/AgCl was applied for 30 minutes to drive electrodeposition. This resulted in thin film samples with a Cu:Fe ratio of 0.6 as determined by ICP-OES analysis. To investigate the effect of removing Cu vacancies, depositions were also performed using a CuNO3 salt concentration of 0.03 M. This yielded a Cu:Fe ratio in the deposited thin film of 1:1 as determined by ICP-OES. Deposited samples were annealed in an air atmosphere for 3 hours at the specified temperature with a ramp rate of 5 °C/min unless otherwise noted. For comparison, select samples were annealed under an Argon atmosphere in a tube furnace using the same ramp rate and a 3-hour dwell time at the specified temperature.

# 2.2 Linear Sweep Voltammetry

A Biologic® SP-50 potentiostat was used for linear sweep voltammetry (LSV) measurements. A warm white-light LED was used as the light source (Thorlabs, MWWHL3). The output of this lamp was collimated, and the power density on the sample was 100 mW/cm². The spectral profile of the white light source is given in Figure S-1. LSV was performed in a glass electrolysis cell with a quartz window to allow for illumination of the working electrode. A 1 M NaOH solution was prepared using 18 M $\Omega$ -cm Millipore water. The electrolyte was purged for 20

minutes with Argon gas prior to experiments. The potential was swept from 0.0 V to -0.8 V vs. Ag/AgCl with a sweep rate of 20 mV/s as the light was modulated on and off with a frequency of 1 Hz.

#### 2.3 Mott-Schottky Analysis

For determination of the flat band potential ( $E_{fb}$ ), Mott-Schottky measurements were performed using a Solatron® Analytical SI 1287 Electrochemical Interface combined with a Solatron® Analytical SI-1260 Impedance/Gain Phase Analyzer. A 1 M NaOH electrolyte solution was prepared using 18 M $\Omega$ -cm Millipore water and the same electrochemical cell was used for these experiments as were used for LSV with a Pt counter electrode and Ag/AgCl reference electrode. A frequency range of 50 mHz to 1 kHz was used with potentials between -0.1 V to 0.8 V vs. Ag/AgCl to determine flat band potentials for each catalyst. The Mott-Schottky Analysis and associated carrier densities appear in Section 11 of the ESM (Figure S-11 and Table S-3 respectively).

# 2.4 Electron Microscopy

A FEI Nova NanoSEM 400 scanning electron microscope was used for imaging the catalysts. This system is equipped with a field-emission gun (FEG) electron source. The Everhart-Thornley detector and an acceleration voltage of 5 kV was used for imaging. Samples deposited on FTO were attached to the sample holder using copper tape. Transmission electron microscopy (TEM) was performed using an FEI Tecnai 30T microscope operating at 300 kV accelerating voltage. Lattice fringes and grain boundaries were evident upon inspection at highmagnification. The pixel/distance ratio was calibrated in Image J and a Fast Fourier Transform was applied to individual regions in Image J to give the approximate d-spacings.

## 2.5 X-ray Photoelectron Spectroscopy

Sample were also analyzed by X-ray photoelectron spectroscopy (Kratos Axis Ultra). A monochromatic Al K $\alpha$  source (hv = 1,486.6 eV) was operated at 120 W with a 12 kV acceleration voltage. The base pressure generated in the ion-pumped chamber was  $1.6 \times 10^{-9}$  mbar. Atomic fractions were determined by peak area fittings followed by normalization to elemental sensitivity factors. Fe 2p spectra were obtained

using a Mg K $\alpha$  source (hv = 1253.6 eV) to avoid potential interference from Cu Auger peaks, which overlap with Fe 2p peaks when an Al anode is used. Spectral fitting was performed with CasaXPS using Gaussian-Lorentzian profiles with a Shirley baseline subtraction.

# 2.6 X-ray Diffraction

A Bruker D8 Advance X-Ray Powder Diffractometer was used to obtain diffraction patterns of the thin film catalysts. A range of  $20^{\circ}$  –  $70^{\circ}$  20 was measured with a step size of 0.02 and a dwell time of 3 sec/step. Data was collected in the Braggs-Brentano mode using Cu K $\alpha$  radiation ( $\lambda$ = 0.15418 nm). The rotation speed was 3 rotations/min with source conditions of 20 kV and 5 mA.

#### 2.6 Raman Spectroscopy

Raman spectra were acquired using a Renishaw inVia Raman microscope with a 632.8 nm HeNe laser (Thorlabs). Raman scattering was directed to the Shamrock 303i spectrograph (Andor) and EMCCD (Newton 970, Andor). High-resolution Raman shift were collected from 187 cm<sup>-1</sup> to 795 cm<sup>-1</sup>. Each spectra was accumulated with an integration time of 140 seconds.

# 2.7 Inductively Coupled Plasma Optical Emission Spectroscopy (ICP-OES)

A Perkin-Elmer Optima 4300 DV Inductively Coupled Plasma Spectrometer was used to collect ICP-OES data for the catalysts to determine the Fe:Cu ratio in the as deposited catalysts. Data was collected for catalysts electroplated from solutions containing a from a 1:1, 1:3, and 1:6 Cu:Fe molar ratio. Once deposited, these catalysts were immediately dissolved in 3 mL of concentrated HCl (Fisher 36.5-38% wt) and diluted with 7 mL of Millipore water. These solutions were then sonicated to ensure mixing and again diluted to 20 mL to ensure the HCl concentration was under 10% wt. Samples as well as blank HCl solutions were prepared in triplicate and the concentration was determined using a calibration curve.

#### 2.8 Visible Light Transient Absorption

The details for visible light transient absorption (TA) measurements have been reported previously [32].

To summarize, a Ti: sapphire amplifier (Coherent Astrella) produced 8 mJ, 35 fs pulses centered at 800 nm with a 1 kHz repetition rate. 3 mJ of the fundamental beam is used to produce a tunable pump pulse, while a white light probe pulse was generated by focusing 1.5 mJ of the fundamental 800 nm beam into a 1 mm thick CaF2 plate. The CaF2 plate was rotated by 1.5 deg every 3 sec to ensure a uniform white light spectrum (400-700 nm) and to prevent beam damage. In these experiments, all samples were excited with 400 nm light produced by second harmonic generation of the fundamental. This 400 nm pump pulse was focused to a spot size of  $1.3 \times 10^{-2}$  mm<sup>2</sup> with an average power of 2 mW. To ensure that samples tested by TA were of uniform thickness, a single thin film catalyst was deposited on one large FTO substrate, which was subsequently divided into pieces. Each piece was then annealed under the specified conditions prior to TA measurements.

#### 2.9 DFT Calculations

All plane wave DFT calculations were performed using the projector augmented wave pseudopotentials [35] provided in the Vienna ab initio simulation package (VASP) [36, 37]. For both Cu and Fe, the 3p states were included as valence electrons resulting in 17 and 14 valence electrons in the DFT calculations, respectively. We used the R3m space group with ferromagnetic (FM) ordering for bulk CuFeO<sub>2</sub> (the 3R polytype) as the relevant phase for experiments at room temperature. We have tested the bulk properties of CuFeO2 using the Perdew-Burke-Ernzerhof (PBE) functional [38], HSE06 functional [39], PBE0 [40, 41], HSE03 [42, 43], and PBE+U [44] with a range of U values from 2 eV to 10 eV (see Table S3 and Section S9 for more details). We find that HSE06 provides the most accurate results for the band gap in comparison to experiment. A large +U value of 8.5 eV is required to reproduce the experimental band gap of 1.5 eV, but the lattice constants predicted by PBE+U show a larger error than predicted by the PBE functional. The PBE lattice constants a and c are 3.030 A° and 17.335 A°, which agree relatively well with experimental values of a =  $3.031 \text{ A}^{\circ}$  and c =  $17.173 \text{ A}^{\circ}$ [45].

Based on these tests, we have chosen the following procedure for examining defects in CuFeO<sub>2</sub>: (1) use

the PBE functional to relax the atoms in the presence of the defect (with the lattice parameters fixed to the bulk PBE values) with a force criteria of  $0.01 \, \mathrm{eV/\mathring{A}}$  and then (2) perform a single-point HSE06 calculation using the relaxed PBE configuration to obtain charge density and partial density of states. The PBE (HSE06) calculations used a plane wave cutoff of 600 (500) eV. In terms of system size, a  $2 \times 2 \times 1$  unit cell with a corresponding Monkhorst-Pack  $4 \times 4 \times 2$  k-point were employed for all the calculations reported in the paper. We evaluated the Bader charges [46] to examine changes in the oxidation state in CuFeO<sub>2</sub> due to the introduction of a Cu vacancy and O interstitial. The Bader charges were obtained from the program provided by Henkelman and co-workers [47-49].

Using the above procedure, we examined the electronic structure of defect free CuFeO<sub>2</sub> and CuFeO<sub>2</sub> with a single Cu vacancy and a single interstitial O atom. Since all Cu atoms in CuFeO<sub>2</sub> are coordinatively equivalent, we removed a Cu atom randomly to generate the single Cu vacant CuFeO<sub>2</sub>. For the O interstitial, we inserted an additional oxygen at the three-fold hollow site between three adjacent Cu atoms (Section S-10 in the ESM presents additional details on the O insertion and other sites examined). Our preferred configuration for O insertion matches that reported in a recent DFT study of interstitial O in CuFeO<sub>2</sub> [30].

#### 3 Results and Discussion

Figure 1 shows XRD patterns for films annealed at 350, 450, 550, and 650 °C in air. The major peak at  $2\theta = 36$ ° in the samples annealed at 350, 450, and 550 °C in air is assigned as the 012 diffraction of CuFeO<sub>2</sub>, consistent with previous XRD patterns for similarly prepared This confirms that delafossite electrodes [50]. CuFeO2 is the major phase present in each of these airannealed samples. A peak at  $2\theta$  =39.2° is also present, and this peak is assigned to the 111 diffraction peak of CuO [27, 28, 51]. Interestingly, this CuO phase coexists with CuFeO<sub>2</sub>, even though the net stoichiometry of the films is Cu deficient as measured by ICP-OES (Cu:Fe = 0.6). We interpret this as evidence of Cu vacancies in CuFeO2, which are required to reconcile a CuO/CuFeO2 mixed phase in a film having a net Fe-rich stoichiometry.

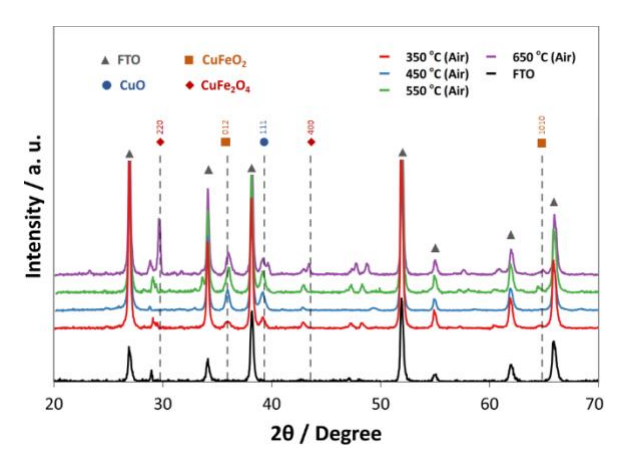


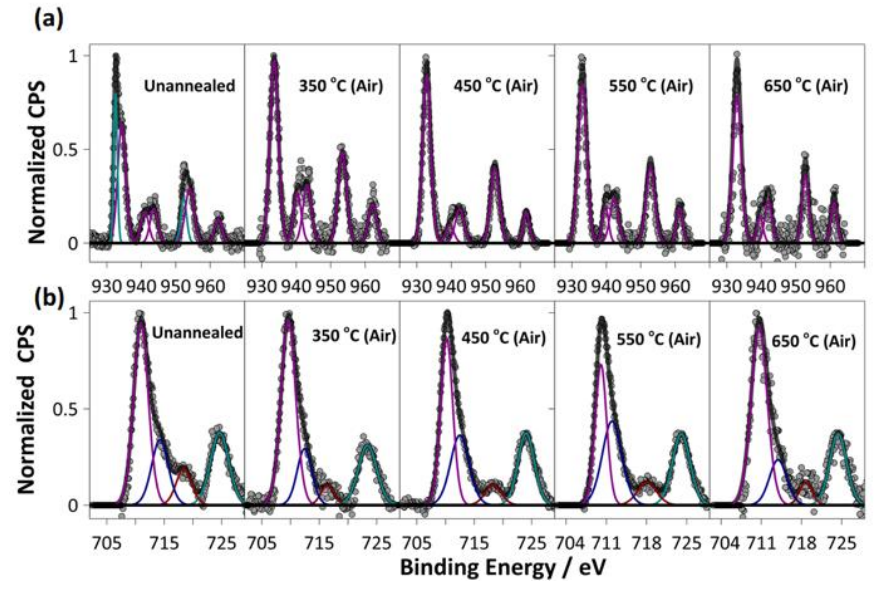
**Figure 1.** XRD patterns of films annealed between 350 and 650 °C in air.

Here we focus on films possessing a Cu deficient stoichiometry, which enables us to explore the effects of Cu vacancies spanning phase compositions from CuFeO<sub>2</sub> to CuFe<sub>2</sub>O<sub>4</sub>. By changing the Cu:Fe ratio of the plating solution, we have also prepared stoichiometric, phase-pure CuFeO<sub>2</sub>. XRD, photocurrent, and visible light TA measurements of this pure-phase CuFeO2 catalyst are provided in Section 2 of the ESM (Figure S-2, S-3, and S-4, respectively). These data along with previous studies [32] confirm assignments for the more complex mixed-phase materials described below.

While relatively little change in the XRD pattern is observed between the 350, 450, and 550 °C samples, a new intense peak appears at  $2\theta$  =29.7° in the 650 °C film, which is assigned as the 220 diffraction of spinel CuFe<sub>2</sub>O<sub>4</sub> [54, 55]. This is consistent with previous observations of a partial phase transition from delafossite CuFeO2 to spinel CuFe2O4 at 500 °C [56]. The exact temperature for this phase transition depends on oxygen partial pressure and film Here this transition can be stoichiometry [55]. explained due to increased Cu vacancy formation at higher annealing temperature until Cu deficient CuFeO2 eventually converts to CuFe2O4. results are consistent with Raman spectroscopy of these materials appearing in section 3 (Figure S-5) in the ESM.

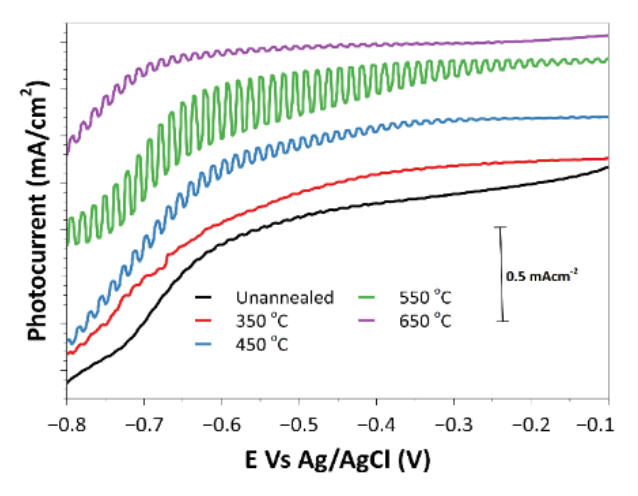
SEM images for each sample are provided in Figure S-6 in the ESM, showing that film morphology is relatively constant for samples annealed between 350 and 650 °C. A TEM analysis of the sample annealed at 550 °C is also provided in Figure S-7.

Figure 2 shows XPS spectra of the Cu 2p (a) and Fe 2p (b) XPS lines for these samples. Analysis of the Cu 2p XPS spectra show that the unannealed sample shows contributions of both  $Cu^{1+}$  and  $Cu^{2+}$  [57]. In contrast, the air annealed samples show primarily  $Cu^{2+}$  with almost no contribution from  $Cu^{1+}$ . This can



**Figure 2.** A. XPS spectra at the Cu 2p-edge. Unannealed sample shows the presence of significant  $Cu^{+1}$  (cyan) as well as  $Cu^{+2}$  (magenta). All samples annealed in air predominantly show the presence of  $Cu^{2+}$ . (B) XPS spectra at the Fe-2p edge. All the samples show primarily Fe<sup>3+</sup> and the Fe oxidation state is negligibly influenced by the annealing conditions.

be seen in the fitting of the fitting of the  $2p_{3/2}$  and  $2p_{1/2}$  XPS lines, which shift from 932.2 and 952 eV to 933.9 and 954.2 eV, respectively. We also observe that the relative intensity of the  $Cu^{2+}$  satellite peaks at 940 and 961 eV increase in the air annealed samples, indicating primarily  $Cu^{2+}$  at the surface of these films.



**Figure 3.** Linear sweep voltammetry of samples for performed in 1M NaOH during illumination with a chopped light source (100 mW/cm<sup>2</sup>).

Depth profiling XPS measurements allow us to observe the change in Cu oxidation state as a function of distance from the surface. These measurements have been reported previously and show that Cu<sup>2+</sup> in these films is localized primarily to the top few nm of the sample and that the subsurface XPS spectra show primarily Cu<sup>1+</sup>, consistent with the nominal oxidation state of Cu ions in CuFeO<sub>2</sub> [33]. XPS of a 550°C Air annealed sample following electrochemical measurements appears in Figure S-12 of the ESM.

Two possible reasons exist for the presence of Cu<sup>2+</sup> at the surface of these samples. First, this may be the result of a CuO phase, which is also detected in the XRD pattern and which may surface segregate during the annealing process. However, if this were true, we would expect to observe an increase in the Cu:Fe ratio compared to the bulk stoichiometry, and this is not the case. Rather, the Cu:Fe ratios measured by XPS are uniformly lower for all samples than the same atomic ratios in the bulk measured by ICP-OES (see tables S-1 and S-2 in the ESM), and these data indicates that Cu does not surface segregated during annealing. Alternatively, it is known that both Cu vacancies and O interstitials serve as p-type donors in CuFeO<sub>2</sub> [12, 56]. If the holes contributed by these

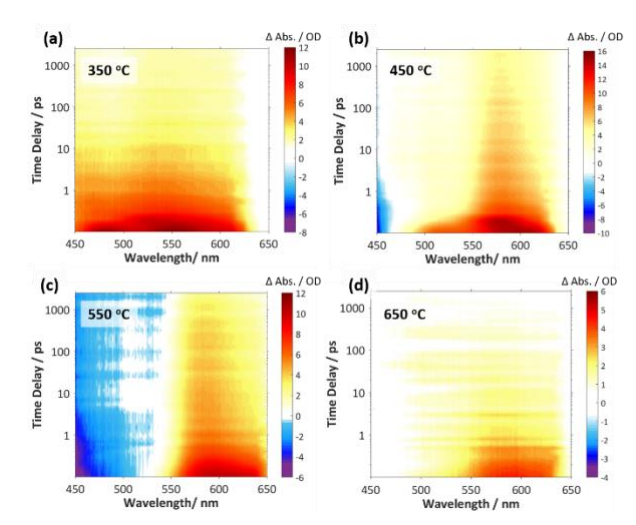


**Figure 4.** Contour plots of UV-Vis transient absorption spectroscopy measurements photoexcited at 400 nm. The time delays are shown in a log scale for 350°C (a), 450°C (b), 550°C (c), and 650°C (d).

defects localize to Cu 3d valence band states, this will result in the oxidation of Cu<sup>1+</sup> to Cu<sup>2+</sup>. Consequently, it is likely that Cu vacancy and/or O interstitial surface defects acting as p-type donors in the CuFeO<sub>2</sub> phase contribute to the presence of Cu<sup>2+</sup> detected at the surface of these samples. In contrast to the Cu XPS, little difference is seen in the Fe 2p XPS spectra between samples (Figure 2b), indicating that Fe is

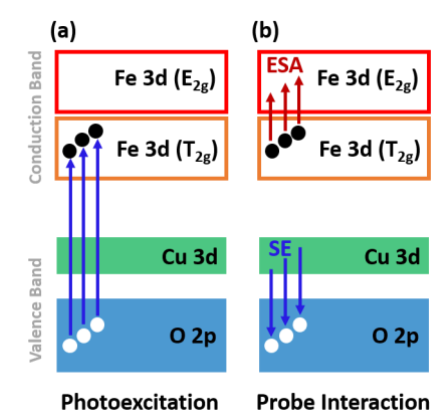


**Figure 5.** (a) Photoexcitation leads to transfer of electron density from the O 2p valence band to the Fe 3d conduction band. (b) Probe interaction following photoexcitation. Excited state absorption (ESA) is associated with inter-band d-d transitions in the Fe 3d conduction band, while stimulated emission (SE) is associated with the inter-band transition from Cu 3d to O 2p in the CuFeO<sub>2</sub> valence band.

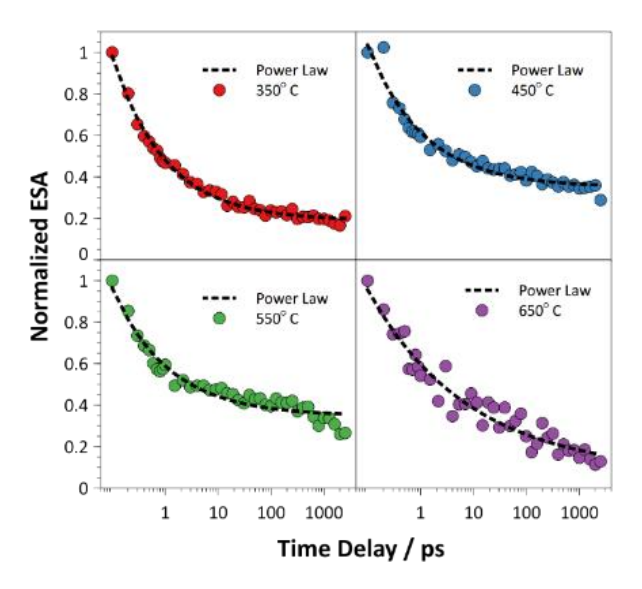
uniformly in the 3+ oxidation state for all catalysts studied here.

Figure 3 shows the result of linear sweep voltammetry measured in 1 M NaOH during illumination with a

chopped light source. We observe that the magnitude of the photocurrent increases with annealing temperature, reaching a maximum of approximately 0.3 mA/cm² for the sample annealed at 550 °C in air. However, upon annealing at 650 °C in air, the photocurrent sharply drops. Figure S-3 in the ESM shows the LSV of a phase pure CuFeO² for comparison. Here we seek to understand the catalyst properties including defect states, which give rise to this observed trend. To better understand the chemical origin of the increased photocurrent density and the influence of specific defects on charge carrier dynamics, we have performed TA spectroscopy of these thin film samples as described below.

The results of the visible light TA experiments where the samples were photoexcited using 400 nm light are shown as contour plots in Figure 4. These plots show TA signal as a function of time delay following photoexcitation in each sample for time delays out to 2 ns. In each sample we observe the presence of a broad excited state absorption (ESA) feature. This ESA feature, which spans nearly the entire measured spectral range in the 350 °C sample, becomes sharper with increasing annealing temperature and is centered at approximately 580 nm in the 450, 550, and 650 °C samples. Additionally, a negative TA signal is also observed at shorter wavelengths only for samples annealed at 450 and 550 °C. Using element specific extreme ultraviolet reflection-absorption (XUV-RA) spectroscopy and DFT calculations, we have recently assigned the origin of these features in CuFeO<sub>2</sub> [32]. As described in that work, the valence band of CuFeO2 consists of both Cu 3d and O 2p character, while the conduction band of CuFeO2 consists primarily of Fe 3d orbitals. Photoexcitation of CuFeO2 at 400 nm produces a charge-transfer state where the photoexcited electron transfers from the O 2p valence band to the Fe 3d conduction band. The ESA feature centered at 580 nm has been assigned as an intra-band transitions of the Fe 3d conduction band in CuFeO2 and represents the signature of photoexcited electrons. This excited state transition is schematically depicted in Figure 5. The origin the negative feature present in 450 and 550 °C is discussed below following analysis of the ESA decay kinetics.

Figure 6 compares the decay of ESA at 580 nm for each catalyst out to 2 ns time delay on a log scale in order



**Figure 6.** Decay of excited state absorption (ESA) at 580 nm as a function of annealing temperature. The black dashed line shows the fit to the experimental data based on power law decay as shown in Equation 1. The time delays on the axis are shown in log scale. Analogous fits based on a stretched exponential model are provided in the Supporting Information.

to show the lifetime of the photoexcited electron in these samples. Associated fits are based on a power law model which we find provides the best match to the experimental data. However, because it can be difficult to extract physically relevant rate constants from power law decay kinetics, we have also performed fits to this data based on a stretched exponential model. We find that the stretched exponential also provides a good match to the experimental kinetics and these fits are provided in the ESM (Figure S-8). Both power law and stretched exponential decay kinetics are consistent with trap state mediated recombination dynamics [58-62], indicating that fast carrier trapping followed by defect-mediated electron-hole pair recombination is the primary pathway for electron relaxation in these materials. Equations describing the power law and stretched exponential decay kinetics are shown in equation 1 and 2, respectively.

$$I(t) = (k \cdot t)^{-b} + c \qquad (1)$$

Here *I*(*t*) represents the normalized time dependent intensity of ESA at 580 nm, k is associated with the rate constant for recombination, b is associated with the order of the decay kinetics, and c is the non-zero offset of the ESA signal.

$$I(t) = e^{-(t/\tau)^{\beta}} + c$$
 (2)

In the stretched exponential model, decay is assumed to proceed by a hopping mechanism, where  $\boldsymbol{\beta}$  is a measurement of the hopping distance relative to the exciton radius and  $\tau$  is the pseudo first order time constant for recombination [63]. Figure 6 and Figure S-8 in the ESM shows that relaxation kinetics for each sample can be described by fast decay of ESA to a state, which is long-lived on the time scale of these measurements represented by the non-zero offset, c. The relative amplitude of this long-lived ESA normalized to the initial transient signal is provided in Table 1. Comparison between samples shows that there is a correlation between the amplitude of the long-lived excited state measured by TA and the observed photocurrent density for each sample as provided in Figure 3 above. This correlation is not surprising since a greater fraction of long-lived carriers is expected to result in a higher photocatalytic efficiency. Therefore, we take the relative amplitude of ESA, which does not decay during the first few ns in this material as an indicator of carrier lifetime and the closely related photoelectrochemical efficiency of the material. We note that while long-lived amplitude of ESA serves a qualitative indicator of photocatalytic performance, additional factors also contribute. These additional variables include changes to the flat band potential and carrier concentration, which are also shown to vary with annealing temperature (see Table S-3 of the ESM).

The visible TA shows the charge carrier dynamics in the bulk, but we acknowledge that surface states may also play a role. We have previously shown by

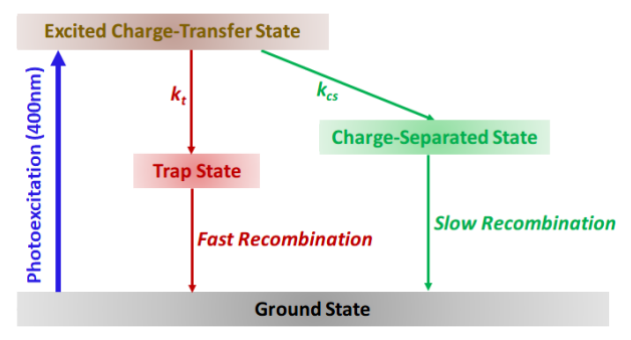


**Figure 7.** Kinetic model showing two competitive pathways for the decay of the excited charge-transfer state. Carrier trapping with a rate constant of  $k_t$  leads to recombination of the excited charge carriers. Charge separation with a rate constant of  $k_{cs}$ , leading to the formation of a long-lived charge-separated state.

surface sensitive XUV-RA measurements that surface dynamics in this material closely follow the bulk, and that the electron thermalizes as a surface-trapped small polaron in the Fe 3d conduction band. In this work we confirm that the photoexcited electrons at the surface persist as small polarons to time delays exceeding 300 ps (see Figure S-13 in the ESM).

To understand the factors that govern carrier lifetime, we consider the fast decay kinetics measured in the stretched exponential model. The values of  $\beta$  and  $\tau$  for each sample are provided in Table 1. Comparing the time constants between samples, we find that a smaller value of  $\tau$  (i.e. faster decay) correlates to a greater ESA amplitude extending to long time delays. At first it may seem counter-intuitive that a fast decay rate leads to a greater carrier lifetime. However, we propose the following kinetic model to explain this observation.

**Table 1.** Fitted time constants( $\tau$ ), hopping parameters ( $\beta$ ) and relative amplitudes (c) to the ESA feature with a stretched exponential function for each sample.

Annealing temperature	Time Constant (τ)	Hopping Parameter $(oldsymbol{eta})$	Amplitude (c)
350 °C	$550 \pm 60 \text{ fs}$	$0.41 \pm 0.03$	$0.23 \pm 0.01$
450°C	$380 \pm 50 \text{ fs}$	$0.38 \pm 0.04$	$0.39 \pm 0.01$
550 °C	$280 \pm 50 \text{ fs}$	$0.35 \pm 0.04$	$0.39 \pm 0.01$
650°C	$1980 \pm 680 \text{ fs}$	$0.26 \pm 0.03$	$0.18 \pm 0.03$

In this model, the photoexcited state can proceed via two competitive pathways shown in Figure 7: In a first pathway, depicted as kt, the carriers trap, leading to subsequent recombination. In an alternate pathway, depicted as kcs, the photoexcited electron and hole separate leading to a long-lived excited state. If we assume that the measured value of  $\tau$  represents an effective rate constant for these two competitive pathways (i.e.  $\tau=1/(k_t+k_{cs})$ ), then a faster rate constant will result from a greater value of kcs leading to more efficient charge separation. We note that the value of  $\beta$  is similar between samples, suggesting that the diffusion distance of trapped carriers is relatively constant across the samples studied here. model can explain why faster initial decay correlates with an overall longer carrier lifetime. more efficient charge separation leads to a greater fraction of long-lived excited states resulting in improved catalyst performance. It should be noted that the faster formation of the chare-separated state means the ultimate slower recombination of the

electrons that leads to the higher photocatalytic performance. We have previously shown that charge separation in CuFeO<sub>2</sub> occurs via ultrafast hole thermalization from O 2p to Cu 3d states in the valence band of CuFeO<sub>2</sub> [32]. This hole thermalization serves to spatially separate electrons and holes across Fe and Cu layers leading to greater carrier lifetime.

To describe how the charge separation process can also be probed by visible light TA measurements, we now consider the origin of the negative feature in the TA data. This feature is only present in the 550 °C sample and to a lesser extent in the 450 °C sample. In CuFeO<sub>2</sub> this negative TA feature has previously been assigned as stimulated emission (SE) from occupied Cu 3d states to photoexcited holes in the O 2p valence band [32], and this process is depicted schematically in Figure 5. According to this picture, the decay of SE in visible light TA measurements corresponds to hole thermalization from the O 2p band to the Cu 3d valence band maximum. This process leads to spatial separation of electrons and holes where electrons remain localized to Fe 3d conduction band states while holes migrate from O 2p orbitals into Cu 3d states. Based on the layered structure of CuFeO2 delafossite, this hole thermalization serves to spatially separate charges across Cu and Fe layers, which weakens the exciton binding energy and facilitate longer carrier lifetimes and increased efficiency. Consistent with this mechanism for charge separation, we find that samples annealed at 350 and 650 °C, which are lacking any features of SE, show no photocurrent. In contrast the samples annealed at 450 and 550 °C do show SE, and both display measurable photocurrent. Compared to films annealed at 450 °C, the films annealed at 550 °C are characterized by a significant increase in the photocurrent density as well as more pronounced SE in the TA measurements. These observations indicate that photoactivity in these samples is closely correlated with charge separation via valence band hole thermalization. Decay of the SE is associated with hole thermalization from the O 2p to hybridized Cu 3d and O 2p valence band leading to spatial charge separation in the layered delafossite structure. This hole thermalization occurs within hundreds of femtoseconds to a few picoseconds. thermalized holes are still excited carriers and are

available to recombine with the excited electrons. The decay of the ESA is associated with the recombination of the excited electrons with the thermalized holes. We note that this ESA feature is long-lived by comparison and due to the separate origin of these two processes is not expected time correlated with the decay of the SE.

We have also considered the possibility that charge separation in these materials is the result of electron transport across internal heterojunctions between CuFeO<sub>2</sub> to CuO. As discussed above, the XRD data reveals the co-existence of CuO and CuFeO<sub>2</sub> phases, therefore charge transfer across a type II heterojunction (CuO/CuFeO<sub>2</sub>) has been proposed as one possible mechanism for the increased excited state lifetime in these mixed phase systems [28, 29]. To investigate this hypothesis, we have measured TA spectra for pure CuO thin films and compare these spectra with CuFeO<sub>2</sub> in order to determine if spectroscopic evidence exists for electron transfer from CuFeO<sub>2</sub> to CuO. Results of TA measurements for pure CuO are provided in Figure S-9 in the ESM.

In summary these data show that that excited states in CuO do not display an ESA feature near 580 nm as observed in the mixed phase CuO/CuFeO2 catalysts. Because this ESA in CuFeO2 is the result of inter-band absorption of photoexcited electrons in the Fe 3d conduction band, electron transfer from CuFeO2 to CuO would lead to decay of the ESA on the time scale of interfacial charge transfer as conduction band electrons are depleted from CuFeO2. However, we instead find that the long-lived amplitude of this ESA feature correlates with improved catalysts activity indicating that electrons in the most active films appear to reside in primarily Fe 3d conduction band Therefore, charge transfer across the states. heterojunction is an unlikely reason for the increased photocurrent in the materials studied here. Together these data indicate that hole thermalization kinetics are primarily responsible for charge separation and carrier lifetime in CuFeO2 samples.

As depicted in Figure 5, the wavelength of SE is related to the energy spacing between Cu 3d and O 2p valence band states. We find that the SE signal is only observed for wavelengths below 460 nm in the 450 °C sample, but shifts to wavelengths as long as 540 nm for the sample annealed at 550 °C. To better

Table 2. Evaluated Bader charges of defect free CuFeO <sub>2</sub> and CuFeO <sub>2</sub> with a Cu vacancy and an interstitial O atom. For the O interstitial,
the 1st neighbor O corresponds to the inserted O. More results of Bader charges can be found in the Supporting Information.

	Cu		Fe		0	
	1st neighbor	2 <sup>nd</sup> neighbor	1st neighbor	2 <sup>nd</sup> neighbor	1st neighbor	2 <sup>nd</sup> neighbor
Defect free	0.62	0.62	1.92	1.92	- 1.27	- 1.27
Cu vacancy	0.77	0.64	1.93	1.92	- 1.25	-1.28
O interstitial	0.93	0.62	1.92	1.92	-1.11	-1.24

understand the origin of this red shift with increased annealing temperature, we turn to DFT calculations, which provide insight into the CuFeO<sub>2</sub> density of states in the presence and absence of Cu vacancy and O interstitial defects.

Cu vacancies and O interstitials represent the primary p-type donors in CuFeO<sub>2</sub>. Figure 8 shows the calculated projected density of states (pDOS) for CuFeO<sub>2</sub>. Part a compares pDOS calculations for defect-free CuFeO<sub>2</sub> with results obtained when a Cu vacancy is introduced into the lattice. Part b shows the same comparison for defect-free CuFeO<sub>2</sub> with results obtained when an O interstitial is introduced into the lattice. It can be seen that neither defect has a significant effect on the Fe 3d states but that both defects have an observable effect on the Cu 3d states. This is consistent with the experimental XPS data (see Figure 2), which shows that the Fe 2p spectrum is

relatively constant with respect to annealing conditions, while the Cu 2p spectrum shows shifts associated with an oxidation state change from  $Cu^{1+}$  to  $Cu^{2+}$ .

Figure S-14 and in the ESM provides information on the potential sites for interstitial oxygen in CuFeO<sub>2</sub>. Table 2 shows the results of DFT Bader charge analysis for nearest neighbor and second nearest neighbor Cu, Fe, and O atoms in the CuFeO<sub>2</sub> lattice. Comparing the Bader charges for defect-free CuFeO<sub>2</sub> with CuFeO<sub>2</sub> containing either a Cu vacancy or an O interstitial shows that neither defect alters the Fe oxidation state. In contrast to Fe, both defects lead to oxidation of neighboring Cu atoms indicating partial hole character on Cu in the presence of these p-type donors. However, the effect of O interstitials on the oxidation state of nearest neighbor Cu is significantly greater compared to the influence of Cu vacancies

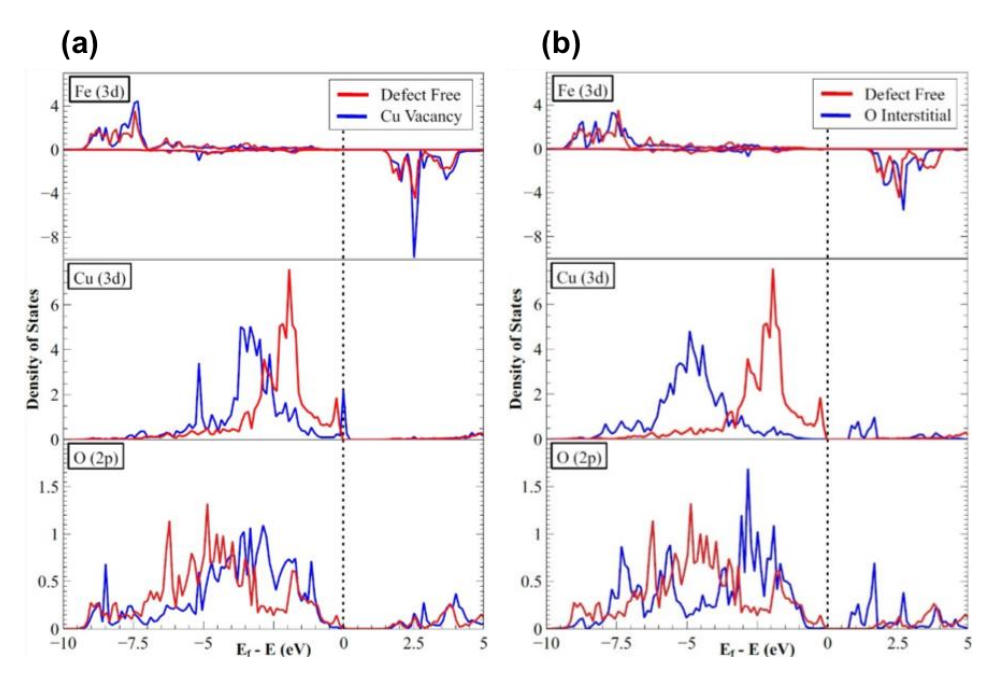


Figure 8. Comparison of partial density of states of (a) defect free CuFeO<sub>2</sub> and Cu vacant CuFeO<sub>2</sub> and b) defect free CuFeO<sub>2</sub> and O interstitial CuFeO<sub>2</sub>.

with Cu Bader charges of 0.77 and 0.93 for Cu vacancy and O interstitial defects, respectively, compared to 0.62 for defect-free CuFeO<sub>2</sub>. We note that the effect of both Cu vacancy and O interstitial defects is found to be extremely local, with second nearest neighbor atoms displaying Bader charges, which are nearly identical to the defect free material. Additional information on Bader charge analysis with respect to various neighboring atoms is provided in Figure S-15 in the ESM. Information on physical properties of CuFeO<sub>2</sub> based on DFT calculation are provided in Table S-4 in the ESM.

Table 3 shows the calculated band centers for Fe 3d, Cu 3d, and O 2p states in defect free, Cu vacant, and O interstitial CuFeO2. From these values, it can be seen that although the Fe 3d conduction band is relatively unaffected, the positions of the O 2p and Cu 3d states are strongly modulated by the presence of Cu vacancy and O interstitial defects. We note that the calculated band centers of Cu 3d and O 2p do not quantitatively predict the position of the stimulated emission of the optical transient absorption. This is not surprising since the optical transient absorption signal consists of partially overlapping ESA and SE features, and the actual intensity of SE will depend on the transition moment integral as well as the joint density of states associated with the valence Cu 3d to valence O 2p band transition. This precludes a quantitative comparison of the absolute position of the band centers from the theoretical calculation; however, here we discuss the qualitative relationship between band center positions and the measured wavelength of SE.

As shown in Figure 8a, the Cu 3d band shifts to lower energy in the presence of a Cu vacancy, while the O 2p band shifts to higher energy. These shifts result in decreased energy spacing between O 2p and Cu 3d valence band states, which is expected to increase Cu-O bond covalency and cause a corresponding red shift in the SE signal. Consequently, the experimentally observed red shift in the SE between samples annealed at 450 and 550 °C is consistent with increased Cu vacancy concentration at higher annealing temperature. The correlation between this red shift in SE signal and the increased photocurrent density suggests that Cu vacancies play

a role in facilitating charge separation by enhancing hole thermalization kinetics.

**Table 3.** Calculated band centers of defect free CuFeO<sub>2</sub>, Cu vacant CuFeO<sub>2</sub>, and O interstitial CuFeO<sub>2</sub>. The centers were evaluated within an energy range from -10 eV to the Fermi level.

	Total	Cu 3d	Fe 3d	O 2p
Defect Free	-4.28	-2.42	-6.57	-4.66
Cu vacancy	-4.57	-3.41	-6.60	-3.87
O interstitial	-4.71	-4.85	-6.70	-4.17

Similar to Cu vacancies, Table 3 shows that O interstitials also result in a shift of the Cu 3d band to lower energy and a shift of the O 2p band to higher energy, and these shifts are even greater for interstitial O compared to Cu vacancy defects. In fact, DFT calculations predict a change in the relative position of O 2p and Cu 3d orbitals upon introduction of an O interstitial defect meaning that the valance band maximum in CuFeO2 changes locally from Cu 3d to O Interestingly, this situation would preclude charge separation based on hole thermalization to Cu 3d states. Accordingly, we predict that O interstitials should have a negative influence on the photoelectrochemical efficiency of CuFeO<sub>2</sub> preventing hole thermalization between layers in These observations can explain why we CuFeO<sub>2</sub>. observe decreased photocurrent, for samples annealed at 650 °C: First, samples annealed at this higher temperature experience a loss of Cu vacancies as Cu-deficient CuFeO2 undergoes a partial phase transition from CuFeO2 to CuFe2O4. Second, O interstitial defects, which increase at higher annealing temperature have a negative effect on charge separation. This explanation for loss photocurrent upon annealing at 650 °C is also consistent with the TA data for this sample, which shows a lack of SE (Figure 4d) and a slow measured time constant, τ, associated with poor charge separation kinetics (Table 1).

## 4 Conclusions

We have considered the possible role of three defects (Cu vacancies, O interstitials, and CuO/CuFeO<sub>2</sub> heterojunctions) in Cu-Fe oxide thin film catalysts and their possible influence on the charge carrier dynamics and photoelectrochemical efficiency. Here we focus on films having a net Cu-deficient stoichiometry in order to consider the role of Cu

vacancies spanning phase compositions from CuFeO<sub>2</sub> to CuFe<sub>2</sub>O<sub>4</sub>. We find that even for CuFeO<sub>2</sub> films having a Cu deficient stoichiometry, CuFeO<sub>2</sub> and CuO are the primary phases observed in the XRD patterns, confirming the presence of Cu vacancies in CuFeO<sub>2</sub>. Photocurrent for these samples is shown to increase with increased annealing temperature from 350 to 550 °C, followed by a sharp loss of photocurrent for films annealed at 650 °C, and this drop correlates with a phase change from CuFeO<sub>2</sub> to CuFe<sub>2</sub>O<sub>4</sub>.

Visible light TA measurements show an excited state absorption at approximately 580 nm for all samples resulting from inter-band excitation of Fe 3d conduction band electrons and that the long-lived state correlates amplitude of this photoelectrochemical efficiency. Kinetic analysis of carrier lifetime shows a fast, sub-ps initial relaxation followed by an excited state having a lifetime greater than 2 ns. Increasing amplitude of the long-lived state correlates with the rate of relaxation. correlation can be understood in terms of a competition between fast charge carrier trapping, which leads to eventual recombination, and charge separation, which leads to enhanced carrier lifetime and improved efficiency. Charge separation is observed spectroscopically as the decay of SE, which results from hole thermalization from O 2p to Cu 3d valence band states. This leads to separation of electrons and holes across layers in the CuFeO2 lattice resulting in increased carrier lifetime and improve efficiency.

Correlation between transient absorption measurements and DFT calculations suggest that Cu vacancies enhance photochemical performance. In contrast, O interstitials lead to a change in the relative positions of O 2p and Cu 3d valence band orbitals, which should inhibit charge separation by inter-band hole thermalization. Finally, we find no evidence for electron injection from CuFeO<sub>2</sub> to CuO suggesting that charge separation at this heterostructure interface does not play a major role in the carrier lifetime or photochemical performance of the catalysts studied here.

#### References

[1] M.G. Walter, E.L. Warren, J.R. McKone, S.W. Boettcher, Q. Mi, E.A. Santori, N.S. Lewis, Solar Water Splitting Cells, Chemical Reviews, 110 (2010) 6446-6473.

- [2] K. Sivula, Metal Oxide Photoelectrodes for Solar Fuel Production, Surface Traps, and Catalysis, The Journal of Physical Chemistry Letters, 4 (2013) 1624-1633.
- [3] K. Sivula, R. van de Krol, Semiconducting materials for photoelectrochemical energy conversion, Nature Reviews Materials, 1 (2016) 15010.
- [4] H. Dotan, K. Sivula, M. Grätzel, A. Rothschild, S. C. Warren, Probing the photoelectrochemical properties of hematite ( $\alpha$ -Fe 2 O 3 ) electrodes using hydrogen peroxide as a hole scavenger, Energy & Environmental Science, 4 (2011) 958-964.
- [5] F.F. Abdi, S.P. Berglund, Recent developments in complex metal oxide photoelectrodes, Journal of Physics D: Applied Physics, 50 (2017) 193002.
- [6] T. Jiang, Y. Zhao, M. Liu, Y. Chen, Z. Xia, H. Xue, Enhancing the Lifetime of Photoinduced Charge Carriers in CuFeO2 Nanoplates by Hydrothermal Doping of Mg for Photoelectrochemical Water Reduction, physica status solidi (a), 215 (2018) 1800056.
- [7] S. Sorenson, E. Driscoll, S. Haghighat, J.M. Dawlaty, Ultrafast Carrier Dynamics in Hematite Films: The Role of Photoexcited Electrons in the Transient Optical Response, The Journal of Physical Chemistry C, 118 (2014) 23621-23626.
- [8] M.S. Prévot, X.A. Jeanbourquin, W.S. Bourée, F. Abdi, D. Friedrich, R. van de Krol, N. Guijarro, F. Le Formal, K. Sivula, Evaluating Charge Carrier Transport and Surface States in CuFeO2 Photocathodes, Chemistry of Materials, 29 (2017) 4952-4962
- [9] U. Kang, S.K. Choi, D.J. Ham, S.M. Ji, W. Choi, D.S. Han, A. Abdel-Wahab, H. Park, Photosynthesis of formate from CO2 and water at 1% energy efficiency via copper iron oxide catalysis, Energy & Environmental Science, 8 (2015) 2638-2643.
- [10] J. Gu, A. Wuttig, J.W. Krizan, Y. Hu, Z.M. Detweiler, R.J. Cava, A.B. Bocarsly, Mg-Doped CuFeO2 Photocathodes for Photoelectrochemical Reduction of Carbon Dioxide, The Journal of Physical Chemistry C, 117 (2013) 12415-12422.
- [11] S. Prévot Mathieu, N. Guijarro, K. Sivula, Enhancing the Performance of a Robust Sol–Gel-Processed p-Type Delafossite CuFeO2 Photocathode for Solar Water Reduction, ChemSusChem, 8 (2015) 1359-1367.
- [12] A. Wuttig, J.W. Krizan, J. Gu, J.J. Frick, R.J. Cava, A.B. Bocarsly, The effect of Mg-doping and Cu nonstoichiometry on the photoelectrochemical response of CuFeO2, Journal of Materials Chemistry A, 5 (2016) 165-171.
- [13] C.G. Read, Y. Park, K.-S. Choi, Electrochemical Synthesis of p-Type CuFeO2 Electrodes for Use in a Photoelectrochemical Cell, The Journal of Physical Chemistry Letters, 3 (2012) 1872-1876.
- [14] Y. Oh, W. Yang, J. Kim, S. Jeong, J. Moon, Enhanced Photocurrent of Transparent CuFeO2 Photocathodes by Self-Light-Harvesting Architecture, ACS Appl Mater Interfaces, 9 (2017) 14078-14087.
- [15] S.H. Yoon, D.S. Han, U. Kang, S.Y. Choi, W. Yiming, A. Abdel-Wahab, H. Park, Effects of electrochemical synthetic conditions on surface property and photocatalytic performance of copper and iron-mixed p-type oxide electrodes, Journal of Materials Science & Technology, 34 (2018) 1503-1510.
- [16] A. Barnabé, E. Mugnier, L. Presmanes, P. Tailhades, Preparation of delafossite CuFeO2 thin films by rf-sputtering on conventional glass substrate, Materials Letters, 60 (2006) 3468-3470
- [17] S. Lee, U. Kang, G. Piao, S. Kim, D.S. Han, H. Park, Homogeneous photoconversion of seawater uranium using copper

- and iron mixed-oxide semiconductor electrodes, Applied Catalysis B: Environmental, 207 (2017) 35-41.
- [18] F.A. Benko, F.P. Koffyberg, Opto-electronic properties of pand n-type delafossite, CuFeO2, Journal of Physics and Chemistry of Solids, 48 (1987) 431-434.
- [19] B.J. Ingram, B.J. Harder, N.W. Hrabe, T.O. Mason, K.R. Poeppelmeier, Transport and Defect Mechanisms in Cuprous Delafossites. 2. CuScO2 and CuYO2, Chemistry of Materials, 16 (2004) 5623-5629.
- [20] A.R.C. Bredar, M.D. Blanchet, R.B. Comes, B.H. Farnum, Evidence and Influence of Copper Vacancies in p-Type CuGaO2 Mesoporous Films, ACS Appl. Energy Mater., 2 (2019) 19-28.
- [21] Y.J. Jang, Y.B. Park, H.E. Kim, Y.H. Choi, S.H. Choi, J.S. Lee, Oxygen-Intercalated CuFeO2 Photocathode Fabricated by Hybrid Microwave Annealing for Efficient Solar Hydrogen Production, Chemistry of Materials, 28 (2016) 6054-6061.
- [22] H.-Y. Chen, G.-W. Fu, Influences of post-annealing conditions on the formation of delafossite—CuFeO2 thin films, Applied Surface Science, 288 (2014) 258-264.
- [23] A.P. Amrute, Z. Łodziana, C. Mondelli, F. Krumeich, J. Pérez-Ramírez, Solid-State Chemistry of Cuprous Delafossites: Synthesis and Stability Aspects, Chemistry of Materials, 25 (2013) 4423-4435.
- [24] S.V. Kalinin, N.A. Spaldin, Functional Ion Defects in Transition Metal Oxides, Science, 341 (2013) 858-859.
- [25] A.J.E. Rettie, M. Sturza, C.D. Malliakas, A.S. Botana, D.Y. Chung, M.G. Kanatzidis, Copper Vacancies and Heavy Holes in the Two-Dimensional Semiconductor KCu3–xSe2, Chemistry of Materials, 29 (2017) 6114-6121.
- [26] C. Rudradawong, C. Ruttanapun, Effect of excess oxygen for CuFeO2.06 delafossite on thermoelectric and optical properties, Physica B: Condensed Matter, 526 (2017) 21-27.
- [27] T. Stöcker, J. Exner, M. Schubert, M. Streibl, R. Moos, Influence of Oxygen Partial Pressure during Processing on the Thermoelectric Properties of Aerosol-Deposited CuFeO2, Materials, 9 (2016) 227.
- [28] U. Kang, H. Park, A facile synthesis of CuFeO2 and CuO composite photocatalyst films for the production of liquid formate from CO2 and water over a month, Journal of Materials Chemistry A, 5 (2017) 2123-2131.
- [29] A. Bera, K. Deb, K.K. Chattopadhyay, R. Thapa, B. Saha, Mixed phase delafossite structured p type CuFeO2/CuO thin film on FTO coated glass and its Schottky diode characteristics, Microelectronic Engineering, 162 (2016) 23-26.
- [30] A. Bera, K. Deb, S. Sinthika, R. Thapa, B. Saha, Chemical modulation of valance band in delafossite structured CuFeO 2 thin film and its photoresponse, Materials Research Express, 5 (2018) 015909.
- [31] C.-M. Jiang, S.E. Reyes-Lillo, Y. Liang, Y.-S. Liu, G. Liu, F.M. Toma, D. Prendergast, I.D. Sharp, J.K. Cooper, The Electronic Structure and Performance Bottlenecks of CuFeO2 Photocathodes, Chemistry of Materials, (2019).
- [32] J. Husek, A. Cirri, S. Biswas, A. Asthagiri, L.R. Baker, Hole Thermalization Dynamics Facilitate Ultrafast Spatial Charge Separation in CuFeO2 Solar Photocathodes, The Journal of Physical Chemistry C, 122 (2018) 11300-11304.
- [33] X. Yang, E.A. Fugate, Y. Mueanngern, L.R. Baker, Photoelectrochemical CO2 Reduction to Acetate on Iron–Copper Oxide Catalysts, ACS Catalysis, 7 (2017) 177-180.
- [34] G. Riveros, C. Garín, D. Ramírez, E.A. Dalchiele, R.E. Marotti, C.J. Pereyra, E. Spera, H. Gómez, P. Grez, F. Martín, J.R. Ramos-Barrado, Delafossite CuFeO2 thin films electrochemically

- grown from a DMSO based solution, Electrochimica Acta, 164 (2015) 297-306.
- [35] P.E. Blochl, Projector Augmented-Wave Method, Physical Review B, 50 (1994) 17953-17979.
- [36] G. Kresse, J. Hafner, Ab initiomolecular dynamics for liquid metals, Physical Review B, 47 (1993) 558-561.
- [37] G. Kresse, Ab initio molecular dynamics for liquid metals, J. Non. Cryst. Solids, 192&193 (1995).
- [38] J.P. Perdew, K. Burke, M. Ernzerhof, Generalized gradient approximation made simple, Physical Review Letters, 77 (1996) 3865-3868.
- [39] A.V. Krukau, O.A. Vydrov, A.F. Izmaylov, G.E. Scuseria, Influence of the exchange screening parameter on the performance of screened hybrid functionals, The Journal of Chemical Physics, 125 (2006) 224106.
- [40] J.P. Perdew, K. Burke, M. Ernzerhof, Influence of the exchange screening parameter on the performance of screened hybrid functionals, J Chem Phys, 105 (1996).
- [41] C. Adamo, V. Barone, Toward reliable density functional methods without adjustable parameters: the PBE0 model, J Chem Phys, 110 (1998) 194101.
- [42] J. Heyd, G.E. Scuseria, M. Ernzerhof, Hybrid functionals based on a screened Coulomb potential, The Journal of Chemical Physics, 118 (2003) 8207-8215.
- [43] J. Heyd, G.E. Scuseria, Efficient hybrid density functional calculations in solids: assessment of the Heyd-Scuseria-Ernzerhof screened Coulomb hybrid functional, J Chem Phys, 121 (2004) 1187-1192.
- [44] S.L. Dudarev, G.A. Botton, S.Y. Savrasov, C.J. Humphreys, A.P. Sutton, Electron-energy-loss spectra and the structural stability of nickel oxide: An LSDA+U study, Physical Review B, 57 (1998) 1505-1509.
- [45] F. Ye, Y. Ren, Q. Huang, J.A. Fernandez-Baca, P. Dai, J.W. Lynn, T. Kimura, Spontaneous spin-lattice coupling in the geometrically frustrated triangular lattice antiferromagnetCuFeO2, Physical Review B, 73 (2006) 220404.
- [46] R.F.W. Bader, Atoms in Molecules: A Quantum Theory, Oxford University Press, Oxford, New York, 1994.
- [47] G. Henkelman, A. Arnaldsson, H. Jónsson, A fast and robust algorithm for Bader decomposition of charge density, Computational Materials Science, 36 (2006) 354-360.
- [48] E. Sanville, S.D. Kenny, R. Smith, G. Henkelman, Improved grid-based algorithm for Bader charge allocation, J Comput Chem, 28 (2007) 899-908.
- [49] W. Tang, E. Sanville, G. Henkelman, A grid-based Bader analysis algorithm without lattice bias, J Phys Condens Matter, 21 (2009) 084204.
- [50] D. Xiong, Y. Qi, X. Li, X. Liu, H. Tao, W. Chen, X. Zhao, Hydrothermal synthesis of delafossite CuFeO2 crystals at 100 °C, RSC Advances, 5 (2015) 49280-49286.
- [51] T. Stöcker, R. Moos, Effect of Oxygen Partial Pressure on the Phase Stability of Copper–Iron Delafossites at Elevated Temperatures, Materials, 11 (2018) 1888.
- [52] W.J. Yu, P.X. Hou, L.L. Zhang, F. Li, C. Liu, H.M. Cheng, Preparation and electrochemical property of Fe2O3 nanoparticles-filled carbon nanotubes, Chem Commun (Camb), 46 (2010) 8576-8578.
- [53] A. Lassoued, B. Dkhil, A. Gadri, S. Ammar, Control of the shape and size of iron oxide ( $\alpha$ -Fe2O3) nanoparticles synthesized through the chemical precipitation method, Results in Physics, 7 (2017) 3007-3015.
- [54] M. Amini, M.H. Kafshdouzsani, A. Akbari, S. Gautam, C.-H. Shim, K.H. Chae, Spinel copper ferrite nanoparticles: Preparation,

characterization and catalytic activity, Applied Organometallic Chemistry, 32 (2018) e4470.

- [55] T. Joshi, T.R. Senty, R. Trappen, J. Zhou, S. Chen, P. Ferrari, P. Borisov, X. Song, M.B. Holcomb, A.D. Bristow, A.L. Cabrera, D. Lederman, Structural and magnetic properties of epitaxial delafossite CuFeO2 thin films grown by pulsed laser deposition, Journal of Applied Physics, 117 (2015) 013908.
- [56] E. Mugnier, A. Barnabé, P. Tailhades, Synthesis and characterization of CuFeO2+δ delafossite powders, Solid State Ionics, 177 (2006) 607-612.
- [57] C. Zhu, A. Osherov, M.J. Panzer, Surface chemistry of electrodeposited Cu2O films studied by XPS, Electrochimica Acta, 111 (2013) 771-778.
- [58] L.M. Carneiro, S.K. Cushing, C. Liu, Y. Su, P. Yang, A.P. Alivisatos, S.R. Leone, Excitation-wavelength-dependent small polaron trapping of photoexcited carriers in  $\alpha$ -Fe2O3, Nature Materials, 16 (2017) 819-825.
- [59] B. Sturman, E. Podivilov, M. Gorkunov, Origin of stretched exponential relaxation for hopping-transport models, Phys Rev Lett, 91 (2003) 176602.
- [60] S.R. Pendlebury, M. Barroso, A.J. Cowan, K. Sivula, J. Tang, M. Grätzel, D. Klug, J.R. Durrant, Dynamics of photogenerated holes in nanocrystalline  $\alpha$ -Fe2O3 electrodes for water oxidation probed by transient absorption spectroscopy, Chemical Communications, 47 (2010) 716-718.
- [61] F.M. Pesci, G. Wang, D.R. Klug, Y. Li, A.J. Cowan, Efficient Suppression of Electron-Hole Recombination in Oxygen-Deficient Hydrogen-Treated TiO2 Nanowires for Photoelectrochemical Water Splitting, J Phys Chem C Nanomater Interfaces, 117 (2013) 25837-25844.
- [62] B. Moss, K.K. Lim, A. Beltram, S. Moniz, J. Tang, P. Fornasiero, P. Barnes, J. Durrant, A. Kafizas, Comparing photoelectrochemical water oxidation, recombination kinetics and charge trapping in the three polymorphs of TiO2, Sci Rep, 7 (2017) 2938.
- [63] B. Sturman, E. Podivilov, M. Gorkunov, Origin of stretched exponential relaxation for hopping-transport models, Physical review letters, 91 (2003) 176602.

#### **Acknowledgements**

This work was supported by the National Science Foundation under NSF award number 1665280. We thank Barbara Dunlap for assistance with TA measurements, which were conducted in the Center for Chemical and Biophysical Dynamics at Ohio State University. We thank Yutichai Mueanngern for assistance with TEM measurements, which were performed in the Center for Electron Microscopy and Analysis at Ohio State University. We acknowledge the Ohio Supercomputing Center for providing computational resources.

## **Electronic Supplementary Material**

Supplementary material (e.g. White light source spectral profile, Characterization of phase-pure CuFeO<sub>2</sub>, Raman spectroscopy, SEM images, TEM

images, Catalyst composition dependence on deposition solution metal ratio, Surface composition by XPS, Stretched exponential fit to the ESA, Timeresolved contour plot of photoexcited CuO and band alignment CuO/CuFeO<sub>2</sub> heterojunction, Comparison of the ESA decay between phase pure CuFeO2 and Cu deficient CuFeO2, Estimation of flatband potential and carrier density, XPS of the 550 °C annealing sample following electrochemical measurements, Time-resolved XUV-RA spectroscopy Quantitative accuracy of the DFT results, Site for interstitial oxygen in CuFeO2, and Bader charge analysis) is available in the online version of this article at http://dx.doi.org/10.1007/10.1007/s12274-\*\*\*-\*\*\*\*-\* and is accessible free of charge.